International Journal of Computer Assisted Radiology and Surgery
https://doi.org/10.1007/s11548-023-02897-z

ORIGINAL ARTICLE

In situ guidance for MRI interventions using projected feedback

Pezhman Foroughi[1] · Alican Demir[1] · Martin Hossbach[1] · Purnima Rajan[1] · Pavel Yarmolenko[2] · Ranjith Vellody[2] · Kevin Cleary[2] · Karun Sharma[2]

Received: 9 March 2023 / Accepted: 29 March 2023

Abstract

Purpose To develop and evaluate an augmented reality instrument guidance system for MRI-guided needle placement procedures such as musculoskeletal biopsy and arthrography. Our system guides the physician to insert a needle toward a target while looking at the insertion site without requiring special headgear.

Methods The system is comprised of a pair of stereo cameras, a projector, and a computational unit with a touch screen. All components are designed to be used within the MRI suite (Zone 4). Multi-modality fiducial markers called VisiMARKERs, detectable in both MRI and camera images, facilitate automatic registration after the initial scan. The navigation feedback is projected directly onto the intervention site allowing the interventionalist to keep their focus on the insertion site instead of a secondary monitor which is often not in front of them.

Results We evaluated the feasibility and accuracy of this system on custom-built shoulder phantoms. Two radiologists used the system to select targets and entry points on initial MRIs of these phantoms over three sessions. They performed 80 needle insertions following the projected guidance. The system targeting error was 1.09 mm, and the overall error was 2.29 mm.

Conclusion We demonstrated both feasibility and accuracy of this MRI navigation system. The system operated without any problems inside the MRI suite close to the MRI bore. The two radiologists were able to easily follow the guidance and place the needle close to the target without any intermediate imaging.

Keywords MRI intervention · Navigation · Guidance · Projector · Tracking · Augmented reality

Introduction

Interventional MRI combines multiplanar cross-sectional imaging capabilities with exquisite soft tissue contrast. MRI guidance has been used for percutaneous needle injections to diagnose and treat neuropathic pain, perform needle biopsy, drainage, tumor ablation, and other clinical indications [1]. The high tissue contrast of MRI makes interventional MRI optimal for lesions that may be difficult to visualize with other modalities such as ultrasound, fluoroscopy, and CT [2]. As currently performed, MRI-guided interventions use an "advance and check" method. This can be challenging, consisting of several steps: (1) initial MRI scan to visualize the anatomy of interest; (2) path planning based on these images; (3) moving the patient out of the scanner bore and manual placement of the needle; (4) moving the patient back into the scanner bore and verification of needle placement with repeat imaging; and finally, (5) taking a sample or injecting a drug. The needle placement and verification steps typically require multiple attempts using the advance and check method and rely on the surgeon's spatial skills to make needle orientation adjustments based on the new images ("cognitive fusion"). These steps take time, especially moving the patient in and out of the scanner bore and re-imaging with each needle advance, while the patient must remain still inside the MRI suite, thereby increasing patient discomfort (and anesthesia duration if used). Such multi-step MRI-guided procedures increase the MRI room time and overall procedure cost and can also cause logistical problems in scanner usage and physician scheduling. Consequently, most interventional procedures in adults are still performed using CT, fluoroscopy, and ultrasound, which do not provide the same image quality as MRI but can be quickly obtained. There is increasing concern about the use of CT imaging and associated ionizing radiation, with over 57 million in-hospital

✉ Pezhman Foroughi
foroughi@clearguidemedical.com

[1] Clear Guide Medical Inc., Baltimore, MD 21211, USA

[2] Children's National, Washington, DC 20010, USA

Published online: 18 April 2023

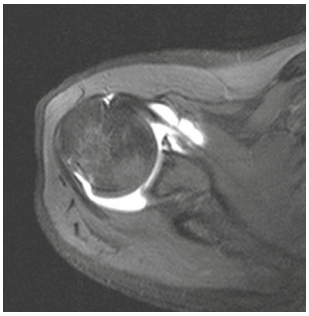

Fig. 1 MRI arthrogram of the right shoulder, transverse plane [5]

scans performed annually in the United States [3]. As radiation exposure concerns continue to rise for both physicians [4] and patients, the use of MRI is increasing, with 18 million in-hospital scans performed annually [3]. In a pediatric setting especially, there is a preference for MRI over CT and X-ray imaging because no ionizing radiation is emitted.

A prime example of MRI-guided interventions is shoulder arthrography shown in Fig. 1, which is on the rise specially for pediatric application. The importance of MRI arthrography in pediatrics stems from the prevalence of children's sports where the surge in intensive training and competition has translated into an increase in musculoskeletal injuries among children [6]. A navigation system designed for MRI intervention may be able to streamline such procedures. Traditional navigation systems which rely on electromagnetic or off-the-shelf optical tracking are not suitable for MRI environment. A main research direction for shoulder arthrography has been an MRI-compatible body-mounted robot under live MRI. The robotic approach can provide great control and visualization [7], but market readiness requires heavy customization due to the complexity involved. (For our purposes, a device is considered MRI-compatible if it is at least "MR Conditional"—i.e., it has been demonstrated to pose no known hazards in a specified MRI environment with specified conditions of use—and the MRI environment affects neither its operating characteristics nor the quality of the images produced) [8].

Another guidance approach which can be used within an MRI suite relies on mirrors. Fritz et. al. [9] discuss an MRI guidance system involving a semitransparent mirror to show the guidance. In Mewes et al. [10], a projector is installed outside of the MRI room and the image is transferred to the scanner bore via a constellation of mirrors. The use of a projector is similar to our approach. However, in practice, utilizing such mirrors in clinical settings is less than ideal and may not be feasible. Also, calibration may be needed before each use and in-bore needle insertion can be ergonomically challenging for the physician, specifically for obese patients. A significant drawback of this work is the lack of live patient tracking to accommodate for rigid motion. Direct error comparisons to our work cannot be made due to the differences in the experimental setup (a flat non-anthropomorphic phantom and multiple mirrors) and absence of detail regarding overall system error and total number of insertions.

Heinrich et al. [11] present a user study comparing three navigation concepts for projective AR-based displays for needle guidance: cross-hair, arrow and circle. In contrast, we provide real-time numerical feedback on the distance to target and intuitive needle orientation guidance by projecting a pseudo-shadow of the needle.

Most other surgical applications of AR systems expect the physician to wear headgear, smart glasses, HoloLens or other hardware. However, the majority of commercially available headgear is not MRI-compatible. Restricted near-range operational distance, lengthy calibration procedures, size and weight of headgear, sterility concerns and inconsistent performance further impact clinical acceptance of the current hardware platforms.

This work describes an augmented reality approach for MRI-guided interventions which provides an intuitive anatomy targeting that is visible to the naked eye. With its MRI-compatible hardware synchronized to the current workflow, the projected on-patient guidance is both easy to use and effective with a clear path to physician acceptance and commercial success.

Methods

System overview

The proposed AR system consists of a medical grade panel PC and an "optical head" that is comprised of two cameras forming a stereo system and a projector. Figures 2 and 7 show the configuration of the system inside the MRI suite.

The optical head is connected to the computational unit via a single USB 3.0 connection which provides both power and data transmission. The computational unit receives high-definition stereo images from the cameras and sends a feedback image to the projector. The optical head is mounted on a passive arm that is attached to either the ceiling or a pole cart holding the PC. The optical head is located above the patient and adjusted to see the area of intervention, similar to the standard operating room lighting. Note that the projector can facilitate correct orientation of the optical unit by highlighting the viewing area.

Workflow

Figure 2 right describes the workflow of a proposed AR/MRI-guided procedure. Prior to imaging, VisiMARKERs are placed on the patient around the intervention area. These markers are visible under MRI, allowing our software to automatically segment them in the MRI volume. The registration

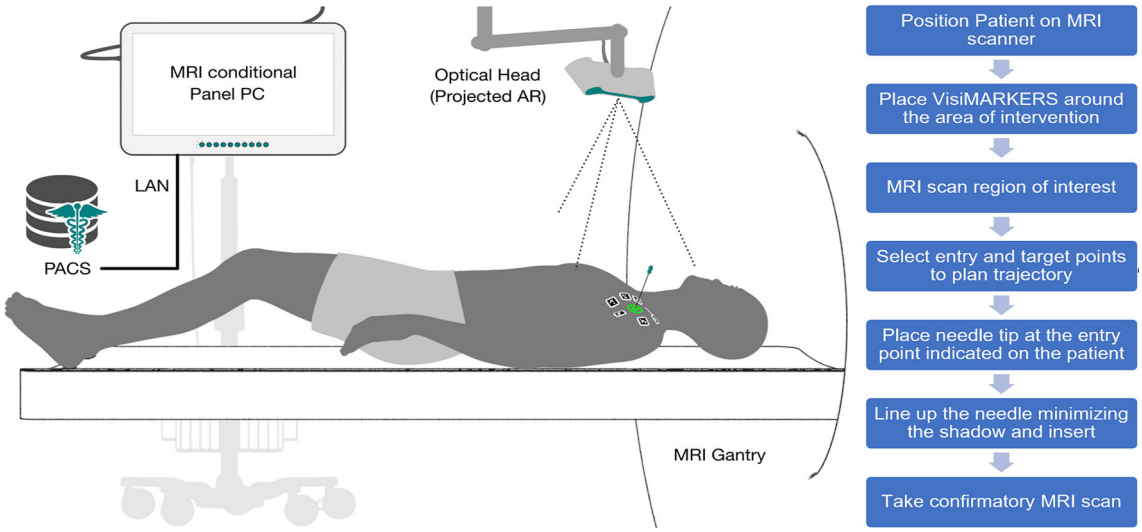

Fig. 2 *Left:* Proposed MRI guidance system comprising of a medical grade panel PC and an optical head for on-patient AR projection. *Right:* The clinical workflow

of MRI volume to camera view happens automatically as soon as the markers come into the field of view. The user then selects an entry point and a target in the MRI image. Given the desired intervention plan, the guidance indicators are projected on the patient helping the physician place the needle tip at the entry point and aligning the needle with the planned trajectory. The projected guidance also shows the progress of the needle toward the target. Note that as shown in Fig. 2, this happens outside the bore, giving the physician easy access to the intervention site. In addition to the projected guidance, a live augmented camera view and cross sections of the MRI volume are shown on the computer monitor. Lastly, a confirmatory volume is acquired to verify the placement of the needle. The following sections describe the major hardware and software components in more detail.

MRI-compatible hardware

Panel PC

The first component is a medical grade panel PC extensively modified to achieve "MR conditional" status beyond the 300 Gauss line for continuous operation in the MRI suite. This is a high-performance 24" touchscreen computer with Intel i7 processor, quad core CPU and 4 GB RAM that handles all computations, data storage, and user input. The modification involved substituting all ferromagnetic structural elements with non-magnetic alternatives. Among those, we replaced the electronics paneling with aluminum alloy due to its lightness, EM shielding performance, and corrosion resistance. Magnetic-driven main speakers were removed from the system, leaving only the non-magnetic piezoelectric buzzer for the sound feedback. All fasteners and standoffs were replaced with their brass and stainless steel counterparts. Certain electronic components, CMOS battery, I/O ports and minor LCD screen components that have weakly magnetic properties were left untouched after verification tests in the MRI suite.

We evaluated the safety of the modified panel PC with a 1.5 T MRI machine. The weakly magnetic components inside the PC were not registered after thorough magnetic sweeps by the MRI safety technologist. The pull force toward the magnet was also measured at 300 Gauss line against an "unmodified" baseline computer of the same model using a Gauss meter and force gauge. No pull force was registered on the modified PC compared to 60 N pull force measured with the unmodified PC.

Optical head

The optical head was designed to be "MR conditional" to operate beyond the 300 Gauss line in an MRI suite. A low-powered projector module with digital light processing (DLP) technology (DLP LightCrafter, Texas Instrument) and off-the-shelf cameras were integrated inside the optical head. This projector has a display resolution of 640 × 360 pixels and a frame rate of 20 fps. The projector module was demagnetized with non-magnetic materials such as stainless steel or aluminum. Even though most projector components were either copper or plastics, the screws and a small heat sink plate were found to be magnetic, all of which are remodeled and replaced. All other optical head electronic components were selected off-the-shelf for low power consumption, small footprint, and minimal magnetic elements. Two standard FLIR 1.3 megapixel Chameleon3 USB 3.0 cameras were employed for the stereo vision system, each with a resolution of 1280 × 1024 pixels and a frame rate of 149 fps.

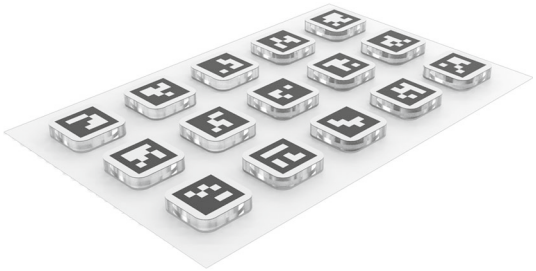

Fig. 3 VisiMARKERs

Fig. 4 TipTAG

A lightweight and MRI-safe stabilizer plate was designed and manufactured to provide a rigid structural base for all electronic components. The stabilizer plate is made from aluminum and acts as a heat-sink for thermal management.

MRI markers

New multi-modality markers that are detectable under both MRI and camera images were designed, developed and assembled in house for accurate, automatic optical localization and registration of the MRI volumes with the camera coordinate frame (Fig. 3). While other research groups have developed multi-modality markers for CT and X-ray imaging [12], there are no multi-modality markers commercially available for MRI.

The developed markers are "MR-safe," sterilizable, and biocompatible for applications on skin. The markers have a medical grade foam adhesive that maintains reliable contact with the skin for extended durations. Each marker is 25 × 25 mm in size. Markers are aseptically packaged in sheets, each of which is carrying a set of 15 rounded square markers with unique "AprilTag" [13] patterns that are machine readable. MRI visibility was achieved using a doughnut shaped synthetic gel, that is encapsulated inside the acrylic body of the marker. The visibility was confirmed under T1-weighted and T2-weighted sequences. The markers were also tested for biocompatibility at a certified microbiological laboratory regarding cytotoxicity and skin irritation with no evidence of adverse effects.

Automatic registration and navigation

There are several software components required to make the proposed workflow possible. The following describes the main components:

Planning UI

We created a utility where the user can browse the MRI images, adjust brightness and contrast, and select a target and an entry point. The planning can be either in axial or lateral plane giving more flexibility to the clinician on how to approach the target.

We also developed the interfaces to send images to the projector via a USB connection thus eliminating the need for an additional HDMI cable to send the guidance images to the projector. This was achieved by setting up a network connection to the projector and sending the images (640×360 pixels) at 20 fps through a TCP/IP connection.

Needle tracking

Active needle tracking is required for this application to provide real-time feedback to the users. We use a "TipTAG" marker-based needle tracking solution (Fig. 4). To make a TipTAG needle, two AprilTag markers are attached back-to-back to the shaft of the needle near the hub. This needle is then shown to the camera system from multiple angles so that the tip location and needle orientation can be calibrated with respect to those markers. Standard pivot calibration was used to calibrate the location of the needle tip with respect to the markers [14]. This process is done only once per needle and can be eliminated in future using an AI approach. The tracking runs at a reduced frame rate of 30 fps using the full resolution 1280 × 1024 images from the stereo cameras.

Marker segmentation

We devised an algorithm which automatically detects and segments the markers in MRI volumes. This is performed in three main steps. First, Otsu thresholding divides the image into background and foreground. It is expected that the markers only reside close to the boundary of the foreground. Therefore, a mask is computed to extract this boundary for the next step. Then, a template is constructed based on the shape and size of the markers. Finally, this template is matched to candidate locations in the volume in 3D to extract both the location and orientation of the markers. In our experiments, the localization error of the localization of the markers compared to manually segmented markers was 0.33 ± 0.19 mm with a detection rate of 98.7% and false positive rate of 0% ($n = 74$).

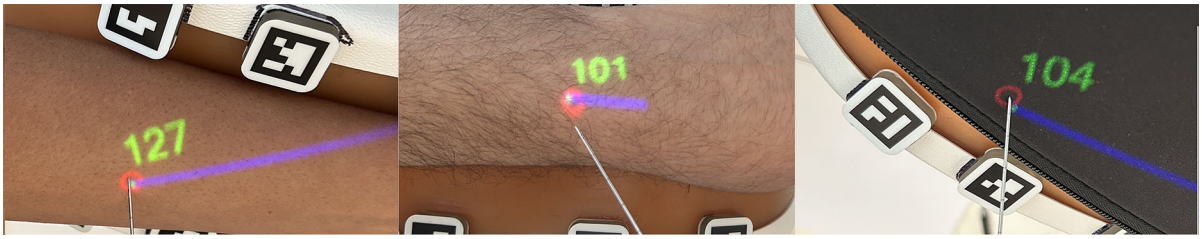

Fig. 5 The projection on varying skin tones and backgrounds

Projected feedback

We implemented the interface to send real-time feedback as images to be projected onto the patient through serial USB connection. The projector and stereo cameras were calibrated using standard calibration routines provided by OpenCV library [15]. The stereo-camera calibration involves collecting a set of image pairs of a checkerboard at several orientations, detecting the corners in each of them, and using these sets of corresponding points to compute the transformation between the two cameras. For projector-to-camera calibration, the projector is simply calibrated in the stereo-camera coordinate system as another camera: a checkerboard pattern is projected on to a plane white board, and the projected corner points are detected in camera images and reconstructed in 3D. Given a collection of 3D points from multiple planes, the intrinsic and extrinsic parameters are computed.

The entry point selected by the user is projected as a small red circle indicating where the tip of the needle should be placed (see Fig. 5). To adjust the orientation of the needle, a virtual shadow is displayed which should be minimized before insertion and while the needle is inserted toward the target. To minimize this line, the user simply reorients the needle away from the projected line as if it is a real shadow. The distance to the target is also displayed both as text and as a circle which its radius shrinks as the needle gets closer to the target (see the supplementary video). The overall projection feedback latency of the system was measured to be around 80 milliseconds.

Integration

Our software can receive MRI volume either via PACS or a USB stick. When an MRI volume is received, it is automatically processed, and the markers are segmented. The stereo camera system continuously processes the stream of images to detect markers. As soon as the patient is moved out of the bore and the markers enter the field of view of the cameras, the markers are detected and automatically registered to the MRI volume. The registration was performed using Horn's method [16], a closed-form solution that computes the best possible transformation between two sets of matching points. This automated process greatly reduces the required user interaction for the intervention while also ensuring that the guidance stays accurate even if the patient moves. The average fiducial registration error (FRE) during our experimentation was 0.3 mm.

Experiment

The test phantom

We created realistic 3D models for the bones and skin surface using open-source shoulder CT images [17]. The 3D models were imported into a 3D printer and using an additive manufacturing technique called stereolithography with an accuracy on the order of 50 μm we achieved exact bone features on the print. The outer shell was printed in a high-temperature resistant resin, and the bones were printed using the modeling resin which has a very high printing accuracy. The bones were then placed in the exact anatomical position and affixed using epoxy (see Fig. 6). The synthetic gel was then melted and dispensed into the outer shell. Two phantoms were made following this process to simulate MRI arthrography procedure during data collection.

Data collection

Two radiologists performed 80 needle insertions over three sessions of experimentation to evaluate the system. As shown in Fig. 7, the guidance system was placed just outside of the 300 Gauss line. We did not have to turn the system off even during scanning and did not observe any interruptions during the data collection due to the strong magnetic field or RF radiations. We used 20 − 22G, 10 cm MRI-compatible needles for all the insertions.

In each MRI session, we obtained an initial MRI scan of one of the shoulder phantoms. Then, the MRI scanning bed was shifted out to bring the phantom into the view of the cameras. The system loaded this scan and automatically segmented and registered the markers. Once a target point and an entry point were selected on the system and the TipTAG needle was calibrated, the radiologist followed the projected guidance to insert the needle. To reduce the MRI

Fig. 6 The custom-built shoulder phantom

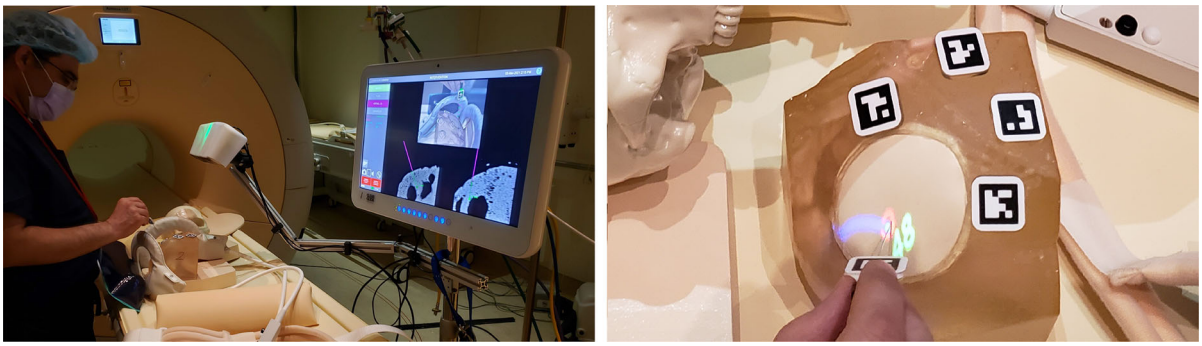

Fig. 7 *Left:* The full system setup in the MRI suite: the panel PC, the projector and the stereo camera head, with the physician inserting the needle into the shoulder phantom; *Right:* The projected guidance cues: the green text indicates the distance to target (48 mm), the red circle is the selected entry point, and the blue line helps orient the needle prior to insertion

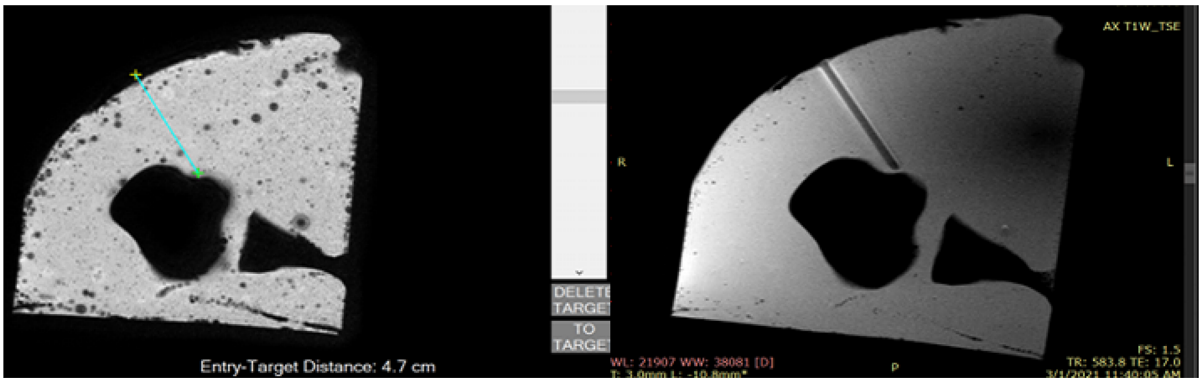

Fig. 8 *Left:* The planned trajectory displayed as a blue line. *Right:* The MR image of the needle post-insertion observed as a black hollow tube

time required for the experiment, the radiologist inserted a second needle aiming for a different target. After each targeting, we logged the data by pressing a button on the system which recorded the needle tip location and the plan. Lastly, we scanned the phantom with the two needles using a metal artifact reduction sequence (Fig. 8 right). Each MRI scan took about 6.5 min, whereas each needle insertion was completed within seconds.

Results

The steps to process the collected data and assess the accuracy were as follows. We first registered the post-insertion MRI scan back to the initial MRI volume on which the entry and target points where selected. This was a rigid registration with at least 4 landmarks manually selected on both volumes. Next, we manually identified the needle tip locations in the registered MRI to establish the ground truth. These needle tip locations were compared to the tip locations and target points recorded by our system. 3D Slicer [18] was used for manual landmark selection, registration, and segmentation of needle tip. Figure 8 shows a sample of the planned trajectory for the needle versus the actual needle path in the post-insertion scan.

Table 1 presents the error values for our experiment. Three error values were calculated:

Table 1 Phantom experiment results from 80 needle insertions

User error (mm)	System error (mm)	Overall error (mm)	Insertion depth (mm)
2.13 ± 0.92	1.09 ± 0.64	2.29 ± 1.12	39.02 ± 5.04

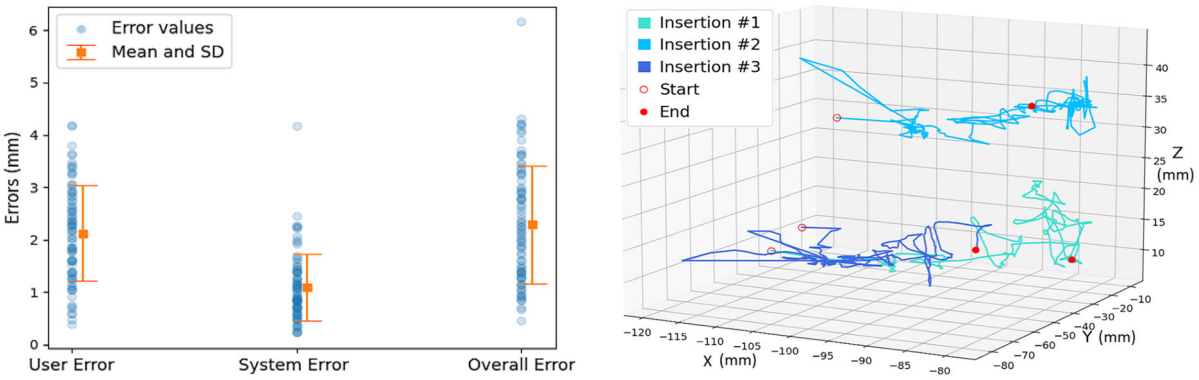

Fig. 9 *Left:* Scatter plot of the 80 needle insertions for 3 types of errors. *Right:* The exemplar spaghetti plots of the needle tip trajectories from 3 different insertions

- User error: the distance between the needle tip and target which was shown to the user. The user tried to minimize this value during insertion.
- System error: the distance between the manually segmented needle tip and the tip location reported by our system. Note that in addition to the error of our system, this error contains manual registration and segmentation error and any unwanted needle displacements as a result of accidentally touching the needle after the insertion.
- Overall error: the distance between the manually segmented tip and the selected target.

Figure 9 left shows the scatter plots for each error type along with their mean and standard deviations for the 80 needle insertions. There is one outlier which is most probably due to accidental displacement of the first needle during the insertion of the second needle before taking the confirmatory scan. Figure 9 right shows exemplar spaghetti plots for the needle tip location for 3 separate needle insertions. Since the area that is targeted for shoulder arthrography is a 10- to 11.5-mm-diameter region around the upper medial quadrant of the humeral head, the overall error from the experiments were deemed acceptable by the collaborating radiologists [19]. The target locations for the 80 insertions were chosen specifically to cover this area comprehensively, as is evident from the large standard deviation of the insertion depth in Table 1. As expected, the system error is lower than the overall error since it does not include the user error. The user error is an indicator of how well the users were able to follow the feedback. The main challenges of computing the error values were the limited accuracy of the confirmatory MRI (due to 2 mm slice spacing of the standard intra-operative sequence and needle artifacts) and "needle push back" where the phantom pushed the needle outward after it reached the target.

Discussion and conclusion

We demonstrated both feasibility and accuracy of this MRI navigation system. The two radiologists were able to easily follow the guidance and place the needle close to the target without any intermediate imaging. The results show that this system is accurate and intuitive. It requires minimal setup and does not significantly modify the clinical workflow making it suitable for wide clinical adoption. Moreover, the relative simplicity of the hardware compared to other MRI navigation solutions paves the way for fast commercialization. Note that the proposed system can also be deployed for CT-guided needle placement procedures extending the impact of this device.

Although all the markers are actively tracked at all times and the guidance is adjusted accordingly, the current system does not take into account internal motions and deformations such as breathing motion. This could be partly remedied in future by modeling the internal motion given a specific procedure such as a lung biopsy and adjusting the feedback accordingly. The projection of guidance seems to be very effective and our initial testing on various skin tones indicate that the efficacy of the system is unaffected. In future, we are planning to add a number of new features including deep learning based markerless instrument tracking and 3D surface reconstruction using structured light. We now intend to translate this system to live clinical practice. This will involve conducting cadaver experiments as a pre-clinical validation step, followed by a first-in-human trial with 12

pediatric patients undergoing MRI-guided soft tissue biopsy and arthrography procedures.

Supplementary information

A video demonstrating how the system works accompanies the paper.

Supplementary Information The online version contains supplementary material available at https://doi.org/10.1007/s11548-023-02897-z.

Funding This work has been supported by NIH Grant Numbers 1R43EB028722-01A1 and 2R44EB028722-02A1.

Declaration

Conflict of interest The authors declare that they have no conflict of interest.

Ethical approval This article does not contain any studies with human participants or animals performed by any of the authors.

Informed consent This article does not contain patient data.

References

1. Ceraulo A, Ouziel A, Lavergne E, Perrier L, Decouvelaere A-V, Chotel F, Thiesse P, Marec-Berard P (2017) Percutaneous guided biopsy for diagnosing suspected primary malignant bone tumors in pediatric patients: a safe, accurate, and cost-saving procedure. Pediatr Radiol 47(2):235–244. https://doi.org/10.1007/s00247-016-3735-3
2. Smith KA, Carrino J (2008) MRI-guided interventions of the musculoskeletal system. J Magn Reson Imaging Off J Int Soc Magn Reson Med 27(2):339–346. https://doi.org/10.1002/jmri.21274
3. Health at a Glance (2019) OECD indicators. OECD Publishing, Paris. https://doi.org/10.1787/4dd50c09-en. Accessed 31 Dec 2019
4. Roguin A, Goldstein J, Bar O, Goldstein JA (2013) Brain and neck tumors among physicians performing interventional procedures. Am J Cardiol 111(9):1368–1372. https://doi.org/10.1016/j.amjcard.2012.12.060
5. Pavic R, Margetic P, Bensic M, Brnadic RL (2013) Diagnostic value of US, MR and MR arthrography in shoulder instability. Injury 44:26–32. https://doi.org/10.1016/S0020-1383(13)70194-3
6. Atay E (2014) Prevalence of sport injuries among middle school children and suggestions for their prevention. J Phys Ther Sci 26(9):1455–1457. https://doi.org/10.1589/jpts.26.1455
7. Lim S, Sharma K, Li P, Petrisor D, Fricke S, Stoianovici D, Cleary K (2019) Robotically assisted long bone biopsy under MRI: cadaver study results. Int J Comput Assist Radiol Surg 14(1):147–156. https://doi.org/10.1007/s11548-018-1889-1
8. FDA MRI Safety. https://www.fda.gov/media/101221/download. Accessed 26 Jan 2023
9. Fritz J, U-Thainual P, Ungi T, Flammang AJ, Cho NB, Fichtinger G, Iordachita II, Carrino JA (2012) Augmented reality visualization with image overlay for MRI-guided intervention: accuracy for lumbar spinal procedures with a 1.5-T MRI system. Am J Roentgenol 198(3):266–273. https://doi.org/10.2214/AJR.11.6918
10. Mewes A, Heinrich F, Kägebein U, Hensen B, Wacker F, Hansen C (2019) Projector-based augmented reality system for interventional visualization inside MRI scanners. Int J Med Robot Comput Assist Surg 15(1):1950. https://doi.org/10.1002/rcs.1950
11. Heinrich F, Joeres F, Lawonn K, Hansen C (2019) Comparison of projective augmented reality concepts to support medical needle insertion. IEEE Trans Visual Comput Graph 25(6):2157–2167. https://doi.org/10.1109/TVCG.2019.2903942
12. Andress S, Johnson A, Unberath M, Winkler AF, Yu K, Fotouhi J, Weidert S, Osgood G, Navab N (2018) On-the-fly augmented reality for orthopedic surgery using a multimodal fiducial. J Med Imaging 5(2):021209–021209. https://doi.org/10.1117/1.JMI.5.2.021209
13. Olson E (2011) Apriltag: a robust and flexible visual fiducial system. In: 2011 IEEE international conference on robotics and automation, pp 3400–3407. https://doi.org/10.1109/ICRA.2011.5979561
14. Yaniv Z (2015) Which pivot calibration? In: Medical imaging 2015: image-guided procedures, robotic interventions, and modeling, vol 9415, pp 542–550. https://doi.org/10.1117/12.2081348. SPIE
15. Bradski G (2000) The openCV library. Dr. Dobb's J Softw Tools Prof Program 25(11):120–123
16. Horn BK, Hilden HM, Negahdaripour S (1988) Closed-form solution of absolute orientation using orthonormal matrices. JOSA A 5(7):1127–1135. https://doi.org/10.1364/JOSAA.5.001127
17. Embodi3D. https://www.embodi3d.com. Accessed 19 Dec 2019
18. Kikinis R, Pieper SD, Vosburgh KG (2014) 3D slicer: a platform for subject-specific image analysis, visualization, and clinical support. In: Jolesz FA (ed) Intraoperative Imaging and Image-Guided Therapy. Springer, New York, pp 277–289. https://doi.org/10.1007/978-1-4614-7657-3_19
19. Crossan K, Rawson D (2022) Shoulder arthrogram. StatPearls Publishing